Simulation of linear polymer melts in transient complex flow

P. Wapperom, R. Keunings

CESAME, Division of Applied Mechanics,
Université catholique de Louvain,
B-1348 Louvain-la-Neuve, Belgium

Abstract

Recently, much progress has been made in improving the modeling of linear polymer melts with the aid of reptation theory. In simple shear flows this has resulted in a much better prediction of the shear viscosity and normal stress ratio. Here we evaluate in complex flow the transient and steady-state behaviour of a recently proposed reptation model, the Marrucci–Greco–Ianniruberto model [1], that includes convective constraint release and a force balance on the entanglement nodes. To incorporate integral type models into the numerical framework of Lagrangian particle methods, developed previously to simulate dilute polymer solutions, we have included the so-called deformation field method. For the contraction/expansion flow that we consider, we find that a correction of the convective constraint release contribution to the relaxation time is necessary to avoid the unphysical situation of negative relaxation times. With this correction, we could obtain mesh and time convergence for high Weissenberg numbers without adding any solvent viscosity. We find that also in complex flow, both the steady-state and transient response of the integral model can be very well approximated by a constitutive equation of differential type. Due to the dominance of the strong thinning in both shear and elongational flows for the model, however, the inelastic Carreau–Yasuda model reproduces the steady-state kinematics and pressure drop as well.

Key words: Lagrangian particle methods; deformation field method; integral models; reptation; contraction/expansion

1 Introduction

Reptation theory [2] has become a basic tool for describing the rheological behaviour of entangled polymers like polymer melts and concentrated solutions. The theory is based on the conceptually simple idea that a polymer chain can move more readily in the direction of its backbone than perpendicular to it. In the latter direction the motion is hindered by neighbouring polymer chains, particularly by entanglements with neighbouring chains. In reptation theory, the resulting constraints are modeled by confining the motion of a polymer chain to a surrounding tube-like region. Although the original model of Doi and Edwards could successfully predict the damping function and the plateau modulus of linear viscoelasticity, it also shows some deficiencies like an excessive shear thinning in fast shearing flows. Recent progress in the modeling of polymer melts has alleviated the shortcomings in the Doi–Edwards model. Proposed extensions include for example stretching of the tube surrounding the polymer chain [3], convective constraint release [4], and fulfilling a force balance on the entanglement nodes [1]. Here, we focus on a model that has recently been proposed by Marrucci *et al.* [1] for linear polymer melts and concentrated solutions. This model includes convective constraint release and a force balance on the entanglements. With these two modifications, a better agreement with experimental data for the shear stress and normal stress ratio could be obtained. It is still an open question, however, how the improved model behaves in more complex flows which we address in the present paper.

The constitutive equations resulting from reptation theory are of integral type, and for the more advanced models developed recently even a double integral is involved. This makes these models computationally much more demanding than differential constitutive equations. In order to avoid numerical simulation with these integral models in complex flow, often an approximate differential constitutive equation is introduced, as for example in [1,5]. In simple flows, these differential equations are able to well approximate the integral models, but for complex flow this has not been established yet.

Recently, the deformation field method has been introduced by Peters *et al.* [6], which allows for efficient simulation of time-strain separable integral models in transient flow. The method represents the history of the fluid deformation by a number of deformation fields, each measuring the deformation between the current time and a certain reference time in the past. With a proper choice of the reference times, the integral can then be accurately approximated by a finite sum of the deformation fields. In a subsequent paper, Peters *et al.* [7] have shown that the method can be extended in a straightforward manner to integral equations that are not time-strain separable and may include double integral models. This allows for simulating the more elaborated reptation models discussed above.

In this paper, we discuss the behaviour of the new model proposed by Marrucci *et al.* [1], called MGI model henceforth, in a benchmark complex flow of a 4:1:4 constriction. As a numerical framework, we take the Backward-tracking Lagrangian Particle Method (BLPM) [8], previously developed for computing differential constitutive equations and kinetic theory models for dilute solutions. The extensions to include the deformation field method into the framework are discussed in Section 3. Besides the behaviour of the MGI integral models in complex flow, we address in Section 4 the quality of an approximate differential equation. Moreover, we compare with the inelastic Carreau–Yasuda model to investigate the role of viscoelasticity for such strongly shear thinning models.

2 Governing equations

For simulation of incompressible and isothermal flow of polymer melts, the standard conservation laws of mass and momentum are used. Additionally, we only consider inertialess flow so that, in the absence of any solvent viscosity for polymer melts, the balance equations reduce to

$$\nabla \cdot \boldsymbol{v} = 0, \tag{1}$$
$$-\nabla p + \nabla \cdot \boldsymbol{T} = \boldsymbol{0}, \tag{2}$$

where $\boldsymbol{v}$ is the fluid velocity, p the hydrodynamic pressure, and $\boldsymbol{T}$ the polymeric stress. The extra-stress tensor $\boldsymbol{T}$ may either be obtained by a micro or macrorheological model. Here, we consider macrorheological models for polymer melts derived from reptation theory. In that case the polymeric stress is governed by a constitutive equation of either integral or differential type.

For the MGI model, the polymeric stress is related to the deformation by

$$\boldsymbol{T} = G \int_{-\infty}^{t} \mu(t;t')\boldsymbol{Q}(t;t')\ \mathrm{d}t', \tag{3}$$

where $G = 6G_0$ with G_0 the plateau modulus and μ is a memory function that depends on the flow conditions. The tensor $\boldsymbol{Q}(t;t')$ denotes a modified orientation tensor at current time t that measures the orientation with respect to a reference time t' in the past. The memory function $\mu(t;t')$ weights the contribution of the orientation tensor $\boldsymbol{Q}(t;t')$ and takes the general form

$$\mu(t;t') = \frac{1}{\tau(t')} \exp\left(- \int_{t'}^{t} \frac{\mathrm{d}t''}{\tau(t'')} \right), \tag{4}$$

where τ is a relaxation time that depends on the flow. In the Doi–Edwards model, τ equals the reptation or disengagement time τ_d. Since τ_d is a constant, the integral can then be calculated analytically and only the integral in Eq. (3) remains to be computed numerically. For more complex models as we use here, however, the memory function has to be calculated as well.

Recently, Ianniruberto and Marrucci [4] have introduced in the reptation model the idea that constraints surrounding a polymer chain are more rapidly swept away in fast flows. To take into account this so-called convective constraint release (CCR), they proposed to take for the overall relaxation time τ

$$\frac{1}{\tau} = \frac{1}{\tau_d} + \frac{\beta}{G}\boldsymbol{\kappa} : \boldsymbol{T}, \tag{5}$$

where β is a numerical coefficient somewhat larger than unity to ensure an increasing shear stress as a function of shear rate. Note that τ is approximately equal to τ_d for slow flows, and that for fast flows the non-linear CCR contribution becomes dominant and considerably decreases the relaxation time. An initially overlooked drawback of Eq. (5) is that the stress work $\boldsymbol{\kappa} : \boldsymbol{T}$ is not strictly positive for viscoelastic models, which may lead to negative relaxation times. For this, we also consider an ad hoc alternative as suggested to us by Marrucci [9],

$$\frac{1}{\tau} = \frac{1}{\tau_d} + \frac{\beta}{2G}\left(\boldsymbol{\kappa} : \boldsymbol{T} + |\boldsymbol{\kappa} : \boldsymbol{T}|\right), \tag{6}$$

which makes the CCR contribution vanish in regions with negative stress work and thus guarantees $0 < \tau \leq \tau_d$.

Instead of solving a double integral, which is computationally expensive, we solve the equivalent evolution equation for μ

$$\frac{D\mu}{Dt}(t;t') = -\frac{\mu(t;t')}{\tau}, \tag{7}$$

where D/Dt denotes the material derivative, with initial condition

$$\mu(t';t') = \frac{1}{\tau(t')}. \tag{8}$$

This is analogous to the approach of Peters *et al.* [7] for the Mead–Larson–Doi model. For reasons of efficiency, the memory function is split in a part that depends on time only and a contribution of convective constraint release which also varies in space, $\mu = \mu^t \mu^{\mathrm{CCR}}$, with $\mu^t(t',t) = \exp\left(-(t-t')/\tau_d\right)/\tau_d$.

The corresponding differential equation and initial condition for the CCR contribution to the memory function then becomes,

$$\frac{D\mu^{\mathrm{CCR}}}{Dt} = -\mu^{\mathrm{CCR}}\frac{\beta}{G}\boldsymbol{\kappa} : \boldsymbol{T}, \tag{9}$$

$$\mu^{\mathrm{CCR}}(t';t') = 1 + \tau_d\frac{\beta}{G}\boldsymbol{\kappa} : \boldsymbol{T}. \tag{10}$$

In case we use Eq. (6) instead of Eq. (5), the evolution equation and initial condition (9) are modified accordingly.

In the Doi–Edwards model, the orientation tensor $\boldsymbol{Q}$ denotes the average orientation of the tube segments. In a recent paper, Marrucci [1] argued that a force balance on the entanglement nodes should be fulfilled, resulting in a modified $\boldsymbol{Q}$ tensor. In this manner, a better agreement with experimental data for the normal stress ratio could be obtained. The modified $\boldsymbol{Q}$ tensor is given by

$$\boldsymbol{Q} = \frac{\sqrt{\boldsymbol{B}}}{\mathrm{tr}\,\sqrt{\boldsymbol{B}}}, \tag{11}$$

where $\boldsymbol{B}$ denotes the Finger tensor that is a measure of the deformation of a fluid element and fulfills the evolution equation

$$\frac{D\boldsymbol{B}}{Dt} = \boldsymbol{\kappa}\cdot\boldsymbol{B} + \boldsymbol{B}\cdot\boldsymbol{\kappa}^T. \tag{12}$$

Note that, because of the scaling in Eq. (11), the stress in Eq. (3) fulfils $\mathrm{tr}\,\boldsymbol{T} = G$ since the integral of the memory function is normalised to one.

As integral models are computationally more expensive than differential constitutive equations, a differential approximation of Eqs. (3), (4), and (12) has been derived [1], by considering a step strain deformation and finding an equivalent differential form for the integral equation. The result is a differential equation for the square of the stress,

$$\frac{D\boldsymbol{T}^2}{Dt} = \boldsymbol{\kappa}\cdot\boldsymbol{T}^2 + \boldsymbol{T}^2\cdot\boldsymbol{\kappa}^T - 2\boldsymbol{T}^2\left(\boldsymbol{\kappa} : \boldsymbol{T}/G\right) - \frac{2}{\tau}\left(\boldsymbol{T}^2 - \frac{G}{3}\boldsymbol{T}\right), \tag{13}$$

where the total relaxation time τ may again be given by Eq. (5) or its positive counterpart (6). It is easily verified, by multiplication of Eq. (13) with $\boldsymbol{T}^{-1}$ and taking the trace, that the differential model fulfils the constraint $\mathrm{tr}\,\boldsymbol{T} = G$ as well.

3 Numerical method

In our numerical method, at each time step, the Eulerian solution of the conservation equations is decoupled from the Lagrangian computation of the polymer stress. In this manner, we can allow for a different solution method well-suited for evolution equations.

The Eulerian form of the equations of motion (1,2) is discretised with the aid of the finite element method. To increase the stability of the numerical scheme, the well-known Discrete Elastic-Viscous Stress Splitting (DEVSS) method [10] has been used. DEVSS involves a separate discretisation of the velocity gradient, which is obtained by projecting the piecewise discontinuous finite element velocity gradient $\nabla \boldsymbol{u}$ on a continuous bilinear field. In the momentum equation, an extra stabilizing term is then included that contains the difference between $\nabla \boldsymbol{u}$ and its projection, multiplied with an auxiliary viscosity η^*. Details about the exact implementation can be found in [8]. For reasons of efficiency, the resulting matrix-vector equation is solved with the aid of an LU factorisation, which only has to be computed once, before the start of the actual flow simulation. Particularly for differential models, this decreases CPU time considerably, of course at the cost of an increase in memory necessary for storing the LU decomposition.

For the computation of the stress integral (3), we use the deformation field method as proposed in [6]. For this method, the past time is represented by a finite number of discrete times $t - t_k$ with $k = 0, \cdots, N_d - 1$, where t_k are the reference times. Because of the fading memory of viscoelastic fluids, the most recent deformations will contribute more to the stress integral than old ones. This can be taken into account by choosing a coarser discretisation for large times, without decreasing the accuracy of the method. Next, to every reference time t_k, a Finger tensor field $\boldsymbol{B}_k(\boldsymbol{x}, t; t_k)$ is assigned, measuring the deformation of the fluid between t_k and the current time t, supplemented with its corresponding CCR memory field $\mu_k^{\mathrm{CCR}}(\boldsymbol{x}, t; t_k)$. The necessary orientation tensors $\boldsymbol{Q}_k(\boldsymbol{x}, t; t_k)$ in the integral are obtained from $\boldsymbol{B}_k(\boldsymbol{x}, t; t_k)$ with Eq. (11). The integrand in Eq. (3) is then approximated by using a finite element discretisation with the nodal values $\mu_k^{\mathrm{CCR}} \boldsymbol{Q}_k$ and basis functions ϕ. This results in a representation of the integral by a finite sum,

$$\boldsymbol{T} = G \sum_{k=0}^{N_d-1} W_k \mu_k^{\mathrm{CCR}}(\boldsymbol{x}, t; t'_k) \boldsymbol{Q}_k(\boldsymbol{x}, t; t'_k), \tag{14}$$

$$W_k = \int_{-\infty}^{t} \mu^t(t; t') \phi_k(t') dt', \tag{15}$$

where the weights W_k do not depend on position. To allow for possible adaptive

time stepping the weights are computed once per time step of the overall scheme. During such a time step, all fields age by Δt so that to avoid a lack of fields for the most current deformations, new fields $\boldsymbol{B}_0(\boldsymbol{x}, t, t)$ and $\mu_0^{\mathrm{CCR}}(\boldsymbol{x}, t, t)$ have to be introduced at every time step. This is done according to the initial conditions $\boldsymbol{B}_0(\boldsymbol{x}, t, t) = \boldsymbol{I}$ and Eq. (10). To keep the total number of deformation and memory fields constant, one of the existing fields is destroyed at every time step as well. Besides, to ensure an accurate method, a proper initial distribution has to be chosen. Details about the initial distribution and the mechanism for the destruction of fields are extensively described in [6]. The specific discretisations we employ here are given in Section 4.

What still remains to discuss is how the time evolution of the N_d fields $\boldsymbol{B}_k$ and μ_k^{CCR} is treated. This is realised by means of a Lagrangian method, the Backward-tracking Lagrangian Particle Method (BLPM) [8]. For Lagrangian particle methods the transport equations, Eqs. (9,12) for the integral model and Eq. (13) for the differential approximation, are solved along the trajectories of Lagrangian particles that are convected by the flow. Along these trajectories the evolution equations reduce to ordinary differential equations. In the first generation Lagrangian Particle Method (LPM) [11] particles are dropped in the flow at the initial time of the simulation, and next these particles are convected by the flow through the whole flow domain. A drawback of LPM is that a large amount of particles is needed in highly graded meshes, resulting in excessive memory and CPU requirements. To circumvent these problems, in BLPM a small number of particle locations are specified a priori in each element of the mesh in which at every time step the Lagrangian data are calculated. To realise this, at each time step, the particle trajectories leading to these positions are calculated by tracking backward in time. In other words, a different Lagrangian particle arrives at a node as time evolves. At the starting point of a trajectory, the Lagrangian data are initialised by interpolation of the nodal values of a stored finite element field at the corresponding time level. Then the equations are integrated with a predictor-corrector scheme to obtain the values of the Lagrangian data at the fixed particle locations in exactly the same manner as for a forward-tracking Lagrangian particle method [11]. In [8] we have shown that tracking only one time step Δt backward in time is sufficient for obtaining accurate solutions, provided the initialisation of the Lagrangian data at the start of a particle trajectory is second-order accurate in space. Here, we take for the fixed particle locations the nodal points of a biquadratic discontinuous finite element representation, which results in nine particle locations per element. Choosing the nodal points has the additional advantage that a least-square fit to map the Lagrangian onto the Eulerian finite element stress becomes superfluous.

4 Results

We consider the start-up flow through a planar 4:1:4 constriction with rounded corners, as depicted in Fig. 1. Around the smallest gap of width H, the con-

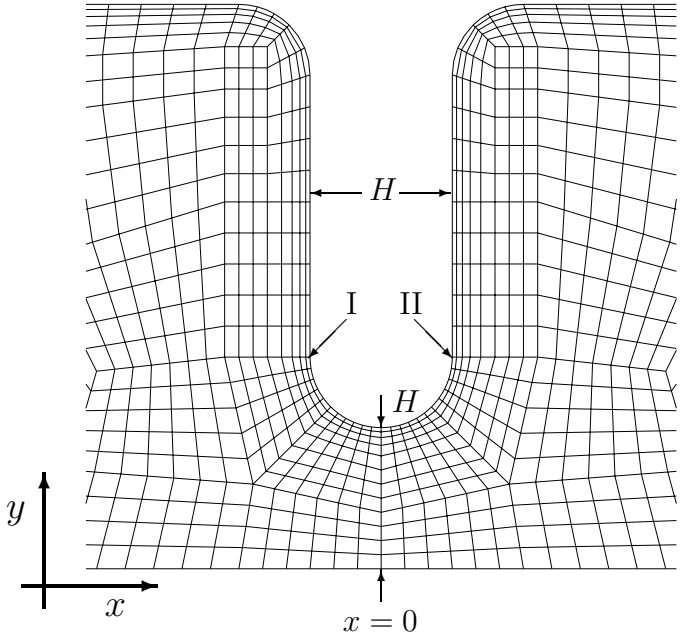

Fig. 1. Zoom of 4:1:4 constriction geometry with rounded corners and medium mesh; indicated are important length scales and points I and II for monitoring stress transients.

striction wall is circular with diameter H. The lengths of the inlet and outlet regions are taken $19.5H$, and at both inlet and outlet we impose fully developed velocity boundary conditions, which have been calculated separately. No-slip velocity boundary conditions are specified at the wall and symmetry conditions hold at the centreline.

We present results for three meshes with quadrilateral elements. The coarse mesh has 564 elements, the area of the smallest element being $\Omega_e = 2.0 \cdot 10^{-2} H^2$. The medium mesh contains 1288 elements, and mainly is more refined near the constriction wall. The smallest element is 10 times smaller, $\Omega_e = 2.0 \cdot 10^{-3} H^2$, approximately a factor 2 parallel and 5 perpendicular to the constriction wall, in order to better capture the very large gradients in the latter direction for flows at high Weissenberg numbers. The fine mesh has again more elements near the constriction wall. In the direction perpendicular to the wall the smallest element size has been decreased by a factor of two, resulting in a smallest element of $\Omega_e = 8.2 \cdot 10^{-4} H^2$. Further away from the constriction, the number of elements has been slightly decreased. A zoom of the medium mesh around the constriction is displayed in Fig. 1.

In all the calculations, we employ a reptation time of $\tau_d = 1$ and a CCR

Table 1
Number of fields N_i per interval and time difference in Δt's in between fields per interval for various time discretisations.

Δt	1	2	4	8	16	32	64	128	256	512	1024	2048	4096
10^{-3}	10	7	9	10	10	10	10	10	10	14	-	-	-
$5 \cdot 10^{-4}$	5	5	7	9	10	10	10	10	10	10	14	-	-
10^{-4}	10	9	9	9	9	9	10	10	10	10	10	10	15

parameter of $\beta = 3.8$, which guarantees an increasing shear viscosity with increasing shear rate [1]. We consider creeping flow, so that in absence of a solvent viscosity, the Weissenberg number is the only characteristic number. We take a Weissenberg number based on the average velocity U at the smallest gap width H, resulting in $We = \tau_d U/H$. Henceforth, all times, coordinates and stresses are expressed relatively to τ_d, H, and G_0, respectively. For the DEVSS method we take the auxiliary viscosity $\eta^* = 6\eta_p$. This high value was necessary to prevent temporal fluctuations in the steady state regime for high Weissenberg numbers. For low Weissenberg numbers and during start up of the flow the same results were obtained as with $\eta^* = \eta_p$.

To discretise the memory integral, the past time $t' \leq t$ is divided into I intervals with increasing time increment. Each interval $i = 0, \cdots, I-1$ contains a number of N_i deformation and memory fields with a time difference of $2^i \cdot \Delta t$ in that interval. The exact values of N_i and the amount of Δt's between the fields in an interval are given in Table 1 for the various time steps. For $\Delta t = 10^{-3}$ and $\Delta t = 5 \cdot 10^{-4}$ we have applied the same time discretisation as proposed in [6]. The total past time spanned by each discretisation is $T = 12.2$ for $\Delta t = 10^{-3}$, $T = 12.2$ for $\Delta t = 5 \cdot 10^{-4}$, and $T = 10.2$ for $\Delta t = 10^{-4}$, respectively. All T are more than the maximum time of 10 after which we stopped all our calculations.

To investigate the influence of viscoelasticity in this flow geometry, we compare results with a generalized Newtonian model possessing only shear-thinning behaviour but no elastic properties. For the Carreau–Yasuda model [12] we consider here, the viscosity is given by

$$\eta = \eta_0 \left(1 + [\lambda I_2]^a\right)^{(n-1)/a}, \tag{16}$$

where I_2 is the second invariant of the rate-of-strain tensor $\boldsymbol{d} = (\boldsymbol{\kappa} + \boldsymbol{\kappa}^T)/2$. The four adjustable parameters in the model are the zero-shear viscosity η_0, a time constant λ, the power-law index n and a numerical parameter a. We have fitted the parameters of the Carreau–Yasuda model on the shear viscosity of the MGI differential approximation. Figure 2 demonstrates that a perfect fit of the shear viscosity can be obtained by using the coefficients $\eta_0 = 1.0$, $\lambda = 1.55$, $n = 0.002$, and $a = 1.8$. With the coefficients obtained from fitting

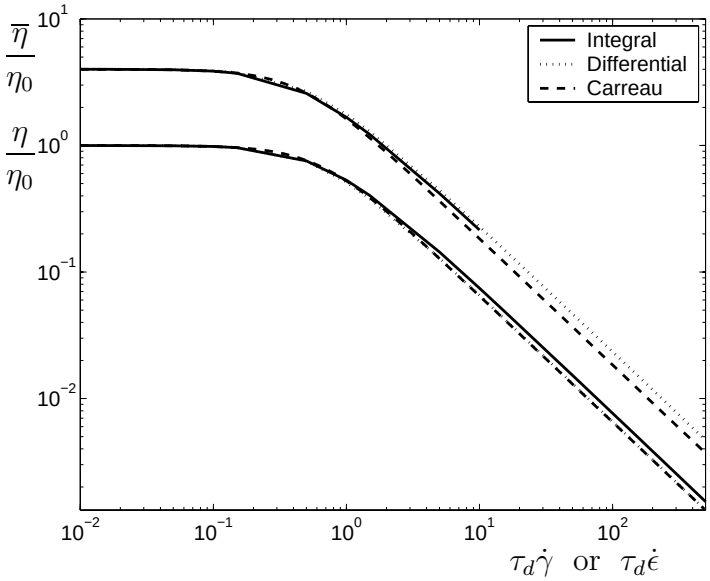

Fig. 2. Shear viscosity η and planar extensional viscosity $\overline{\eta}$ for integral MGI model, its differential approximation, and Carreau–Yasuda model.

the shear viscosity, however, the planar elongation viscosity $\overline{\eta}$ of the Carreau–Yasuda model nearly coincides with the curves for both the differential and integral MGI model as well. The very strong decrease of the overall relaxation time τ, not only for shear but for all type of deformations, seems to strongly decrease all steady viscosities. This means that in the steady state solutions, only differences are expected due to normal stress differences and transient behaviour along the particle trajectories in the constriction. For the inelastic Carreau–Yasuda model the response is instantaneous, while for the viscoelastic models the stress requires time to build up and relax. The impact of the transient behaviour of this model, however, is not clear a priori. As can be observed from Fig. 3, the transient response of the stress tends to approach

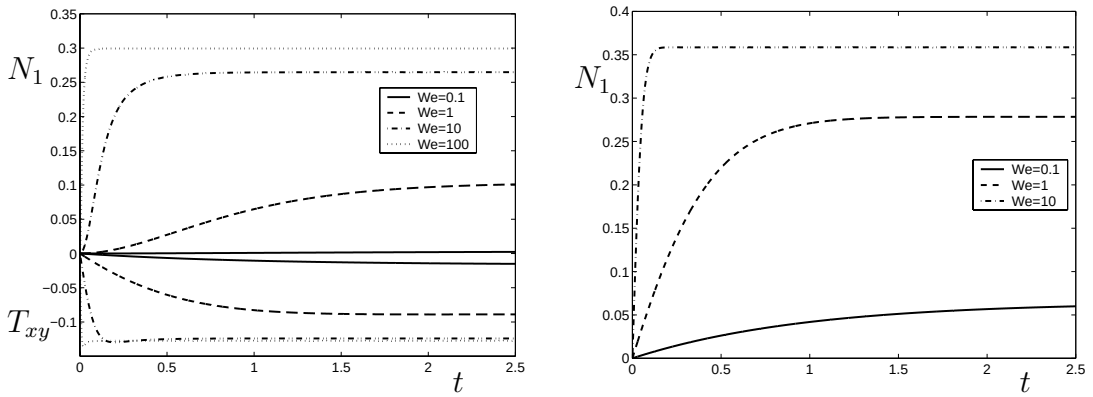

Fig. 3. Transient normal and shear stress of integral MGI model for various Weissenberg numbers; left: start-up of shear, right: start-up of planar extension.

more and more the instantaneous behaviour of an inelastic model. Moreover, this means that steady state is approached very fast for high Weissenberg

number flow. Particularly in planar extension, an instantaneous-like response is already observed for a Weissenberg number of $We = 10$.

For the integral MGI model using a total number of $N_d = 100$ deformation and memory fields, the computer requirements on the medium mesh are 130 MB memory. To store the 100 fields approximately 75 MB is used, while 40 MB is used for the LU factorisation in the solver of the momentum equation. The CPU time was almost 2 seconds per time step on a 667 MHz ev67 processor of a DEC Alpha workstation, which results in an overall CPU time of 5 hours 20 minutes per run for a time step of $\Delta t = 10^{-3}$ and final time of 10. The differential approximation only contains one field instead of the 100 deformation and memory fields, so needing considerably less memory, approximately 50 MB including the 40 MB for the LU factorisation. The CPU time was typically 0.4 seconds per time step, resulting in an overall CPU time of just over 1 hour per run using the same time step and final time. Note the relatively small increase of memory, a factor 2.5, and the CPU-time, a factor 5, for the integral model, whichs reveals the efficiency of the numerical method.

4.1 Mesh and time convergence

Figure 4 shows the transients of normal and shear stress for the integral MGI model at points I and II of Fig. 1. A time step of $\Delta t = 10^{-3}$ has been used,

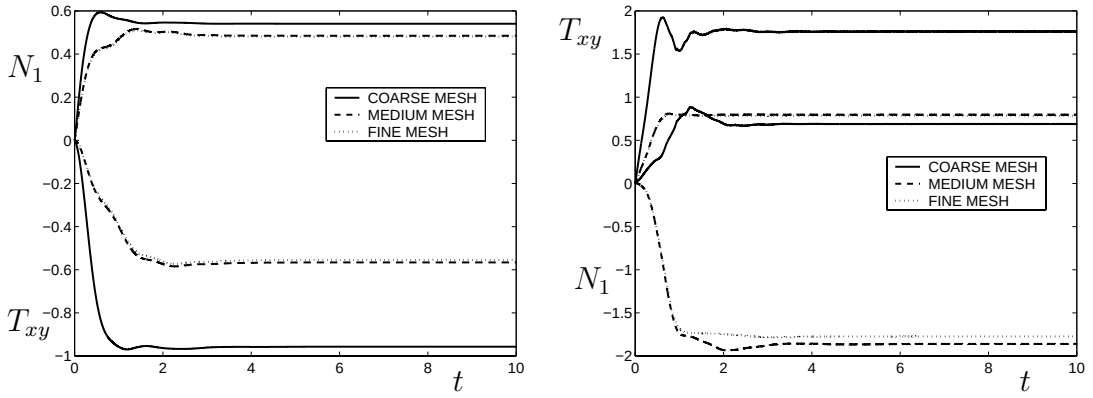

Fig. 4. Mesh convergence of transients of normal stress and shear stress at $We = 3$; left: point I, right: point II.

with $N_d = 100$ fields, using linear basis functions ϕ_k to calculate the weights of Eq. (15). Doubling the number of fields or changing from linear to quadratic basis functions did not give any significant changes in the stress. From Fig. 4 we detect that the coarse mesh cannot accurately represent the solution, particularly at the downstream side of the contraction. Transient stresses for the medium and fine mesh, however, almost coincide, except for a small difference in N_1 of point II. As can be observed from Fig. 5, in which the steady-state normal and shear stress are plotted on the horizontal line through these points,

the small difference is only locally at the boundary on the downstream side. Upstream and in the interior of the flow the results for the medium and fine

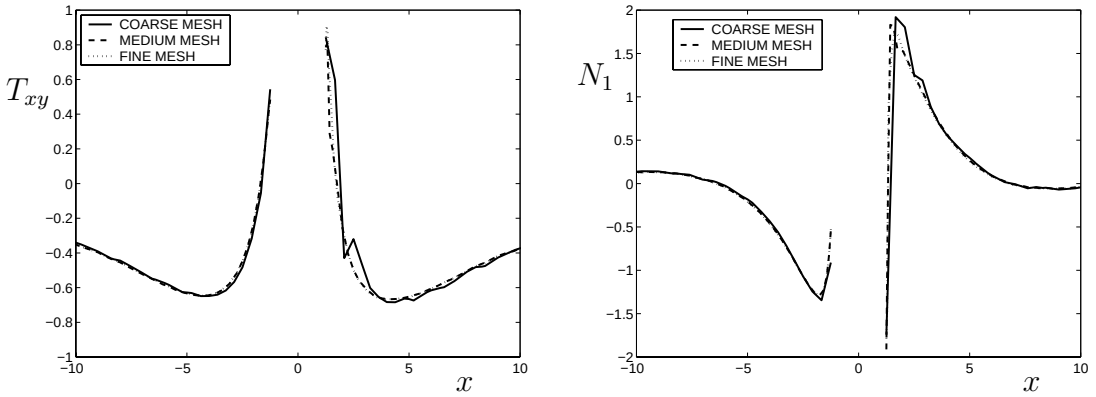

Fig. 5. Mesh convergence for $We = 3$ near constriction for shear stress T_{xy} and normal stress N_1 along the line $y = 3H/2$.

mesh are identical. We therefore conclude from Figs. 4 and 5 that the medium mesh is sufficient to accurately represent the solutions. From Fig. 5 we already note the much steeper gradients in the boundary layer on the downstream side. Because of the finite relaxation time, the large stresses that have developed near the wall in the contraction region have not fully relaxed before the second strong deformation in the expanding region starts. Consequently, higher stress levels can be reached on the downstream side of the constriction.

In Fig. 6 we display for various Weissenberg numbers the mesh convergence of the steady-state pressure drop. We define the pressure drop in the constriction

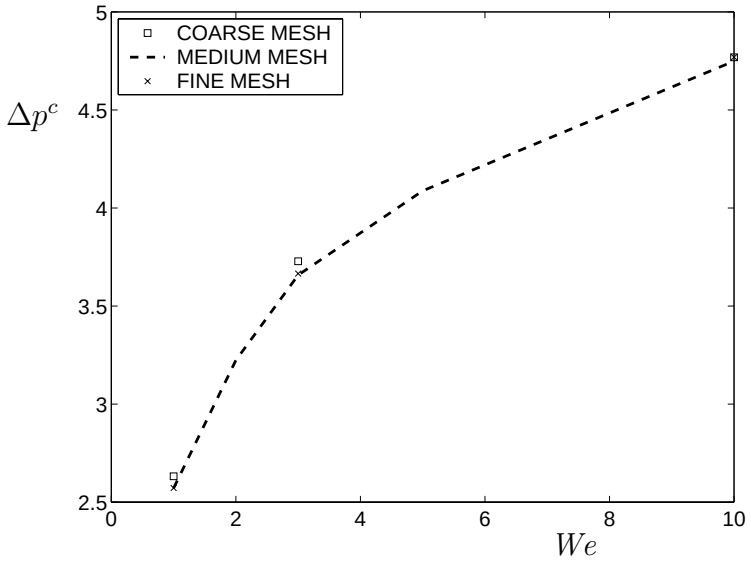

Fig. 6. Mesh convergence for pressure drop in constriction, Δp^c, for integral MGI model as function of Weissenberg number.

as $\Delta p^c = \Delta p - \Delta p^0$, where Δp is the total pressure drop in the flow and Δp^0

the pressure drop corresponding to a fully developed flow in a channel without the constriction, i.e. length $40H$ and width $4H$. Again results for the medium and fine mesh coincide, while there are some small differences with the coarse mesh. Compared to the steady-state values of the stresses in Fig. 4, however, the deviations are rather minimal. This indicates that the pressure drop is not very sensitive to small changes of the stresses in the boundary layer near the constriction wall. Furthermore, note the continuously decreasing slope of the pressure drop curve with increasing Weissenberg number, revealing the dominance of shear thinning of the model.

Figure 7 shows the time convergence of the transients of normal and shear stress for the integral MGI model, again for the points I and II indicated in Fig. 1. The time discretisations are indicated in Table 1. For point I at the

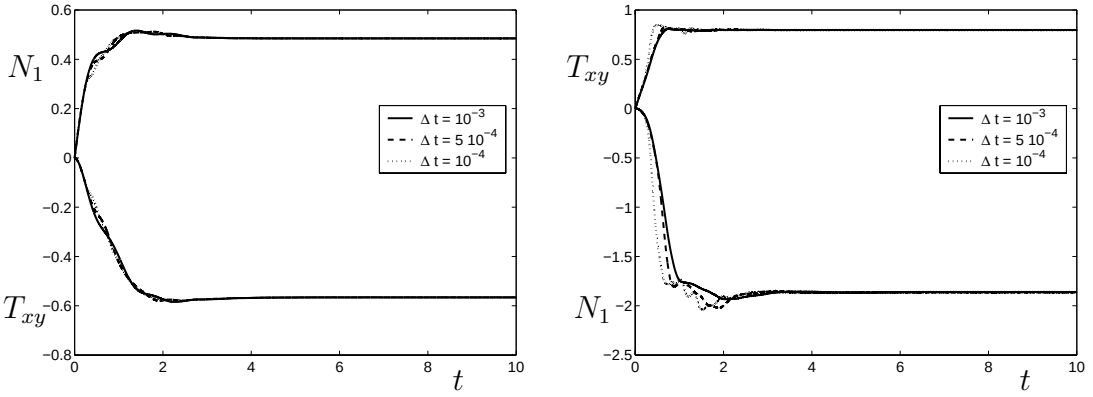

Fig. 7. Time convergence of transients of normal stress and shear stress at $We = 3$; left: point I, right: point II.

upstream side, the three transients nearly coincide. In the steep boundary layer at the downstream side, at point II, we observe some small deviations and temporal fluctuations in the intermediate regime. Initially and particularly at steady state, however, the transients coincide for all three time steps. We conclude that a time step of $\Delta t = 10^{-3}$ is sufficient for further calculations.

4.2 CCR contribution to the relaxation time

We first consider the original MGI integral model of [1], i.e. for which the relaxation time (5) is not strictly positive. The isolines of the extra contribution to the relaxation time due to convective constraint release, $\beta\boldsymbol{\kappa} : \boldsymbol{T}/G$, are displayed in Fig. 8. At a low Weissenberg number of $We = 0.1$, the flow is almost Newtonian. Consequently, the isolines are almost symmetric in the flow direction and the CCR contribution practically remains positive everywhere, since the stress work approximately equals $\boldsymbol{\kappa} : \boldsymbol{T} \simeq 2\eta_0\boldsymbol{\kappa} : \boldsymbol{\kappa}$, which is positive by definition. The maximum value arises at $x = 0$ at the constriction wall, around which the large values are concentrated in a boundary layer. Compared

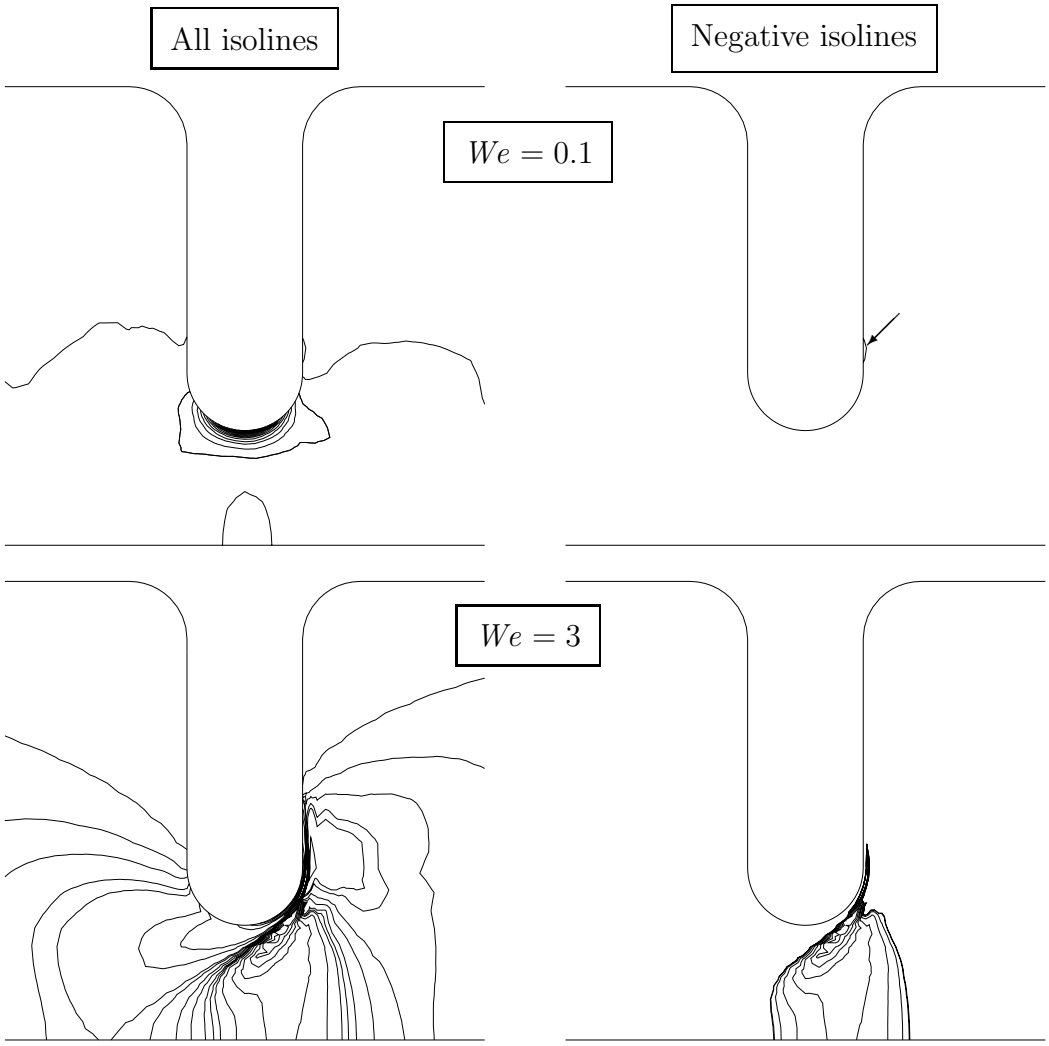

Fig. 8. Isolines of $\beta\boldsymbol{\kappa} : \boldsymbol{T}/G$ for integral MGI model at low and medium Weissenberg number; for clarity negative isolines are also displayed separately on the right-hand side; $We = 0.1$: [-0.002,0.163], $We = 3$: [-4.89,48.4].

to the reptation time $\tau_d = 1$, however, the maximum value of 0.163 for the CCR contribution is still relatively small. At a higher Weissenberg number of $We = 3$ the situation changes dramatically. The maximum is shifted downstream along the wall of the constriction. A large region of negative values develops in the expansion of the flow, extending from the axis of symmetry till close to the constriction wall where very large positive values develop. The reason is the change of sign of the velocity gradient, while the stress does not change sign because of the finite relaxation time. Increasing the Weissenberg number up to 5 resulted in such large negative relaxation times that the simulation blew up. We must remark here that the surprising negative region of the CCR relaxation time before $x = 0$, is caused by the mapping of the piecewise discontinuous data to a bilinear continuous field, necessary in the postprocessing stage for the generation of contour plots. In the boundary layer at the wall, the CCR contribution to the relaxation time dominates over the

reptation time, decreasing the overall relaxation time τ by almost a factor of 50. Immediately next to the boundary layer, τ is larger than the reptation time due to the negative stress work in that region.

Figure 9 shows the impact of the enforcement of positiveness (6) in the CCR

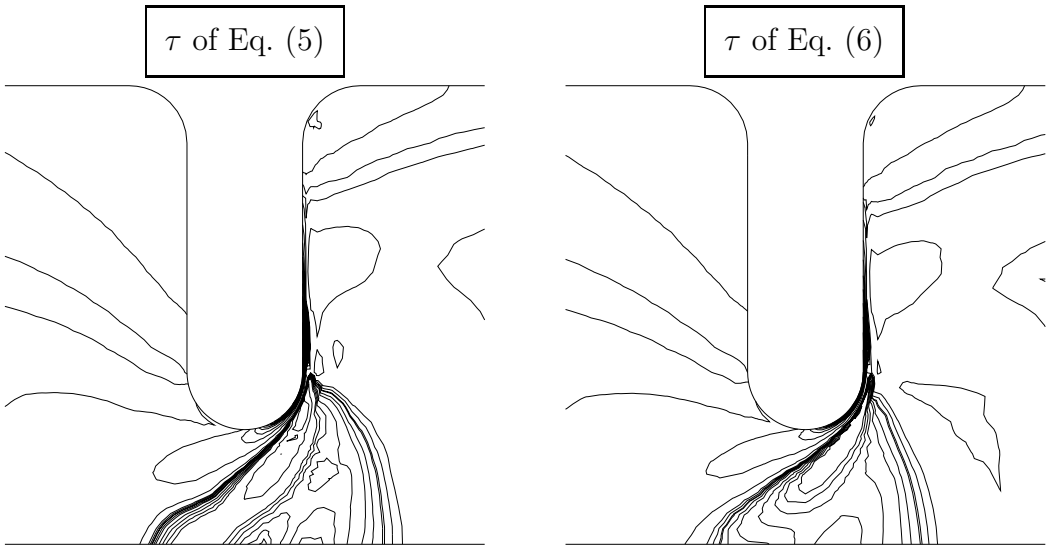

Fig. 9. Isolines of $\beta\boldsymbol{\kappa} : \boldsymbol{T}/G$ for MGI differential approximation at $We = 10$; τ of Eq. (5): [-20.5, 109.0], τ of Eq. (6): [-10.6, 94.1].

contribution of the relaxation time for a high Weissenberg number of 10. Since for these high Weissenberg numbers the simulations blew up using the integral model with the non-positive CCR relaxation time, we only show results for the differential approximation which seems to be less sensitive for this. We observe that outside the region with a negative CCR relaxation time the contour lines are remarkably similar. Inside that region, however, the solutions differ considerably. Only one local maximum exists at the centreline when the strictly positive relaxation time is used while three are observed for the original overall relaxation time of Eq. (5). In view of the extent of the negative region, and the large impact on the result there, it seems worth to include convective constraint release in a more physical manner than the ad hoc alternative (6). Since the non-positive CCR relaxation time obviously leads to unphysical results, we will only consider the positive alternative henceforth.

A comparison between the CCR relaxation time for the MGI integral model and its differential approximation at $We = 10$ is provided in Fig. 10. From this figure we gather that even in this complex flow, the differential model is a very good approximation of the integral version for high Weissenberg numbers. Particularly upstream of the constriction, in the zero region, and in the boundary layer, the contours are almost identical. At the downstream side some small differences appear in the region where the relaxation takes place. The overall pattern, however, remains very similar. Results at lower

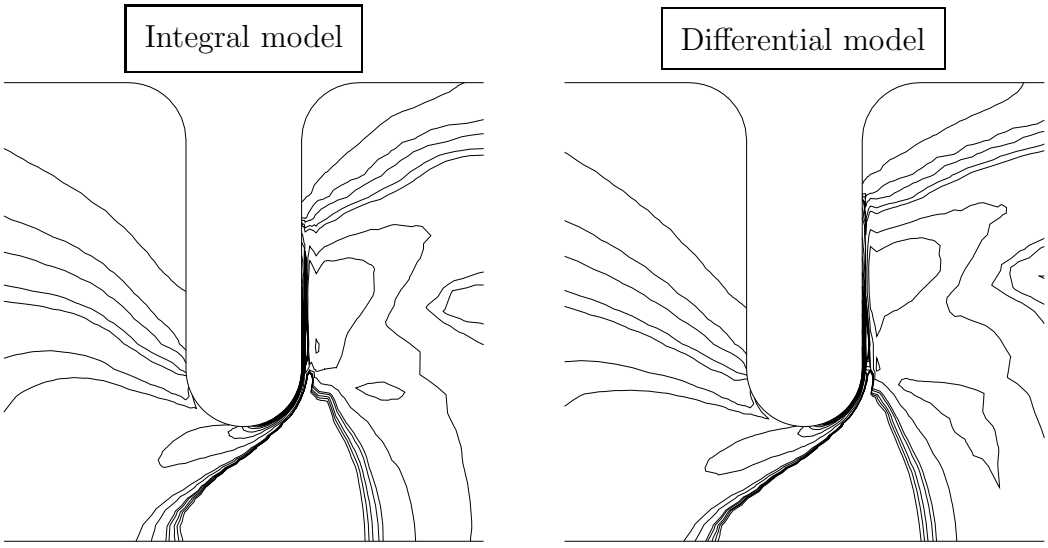

Fig. 10. Isolines of CCR relaxation time for integral MGI model and differential approximation at $We = 10$ using Eq. (6); integral model: [0, 112], differential approximation: [0, 94.1].

Weissenberg numbers, not shown here, agree evenly well.

4.3 Comparison with Carreau–Yasuda model

To investigate the influence of viscoelasticity on the pressure drop, we consider the pressure drop in the constriction Δp^c, non-dimensionalised with the pressure drop in a straight channel Δp^0. Results for this non-dimensional pressure drop obtained with the various models are shown in Fig. 11. Since the inelatic Carreau–Yasuda model possesses no viscoelasticity, results are presented as function of the non-dimensionalised average velocity V^* in the constriction. Because we used τ and the gap half-width H for the non-dimensionalisation V^* takes the form of the Weissenberg number for the viscoelastic models. The Carreau–Yasuda model predicts the pressure drop well up to high Weissenberg numbers of the viscoelastic models. Remarkable is that the inelastic model resembles the integral MGI model more closely than the differential approximation, for which the pressure drop slightly increases for higher Weissenberg numbers. The surprising correspondence between the integral model and the Carreau–Yasuda model seems to be coincidental, since the shear viscosity of the Carreau–Yasuda fit in Fig. 2 resembles the differential model more closely.

Figure 12 compares the steady-state shear and normal stress at $We = 3$ for the integral model, the differential approximation, and the Carreau–Yasuda model. The stresses are plotted along the line $y = 3H/2$, i.e. through the points I and II, indicated in Fig. 1, at the end points of the circular part of the constriction. For the inelastic Carreau–Yasuda model the stresses are

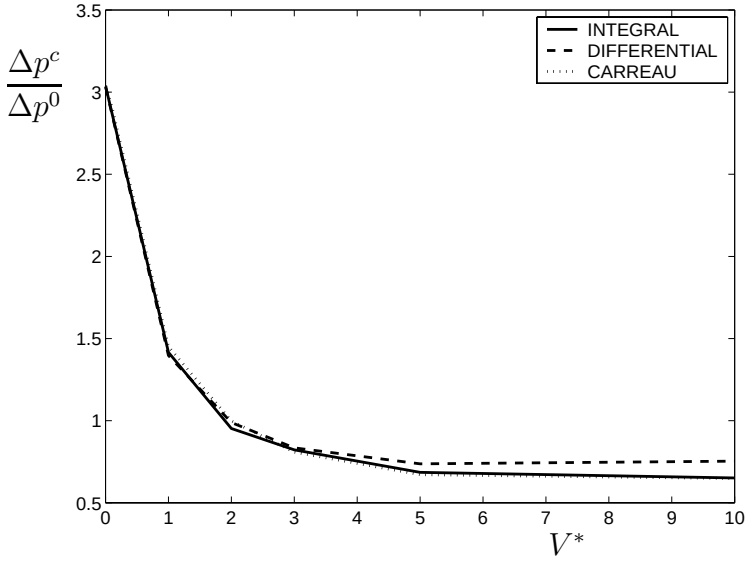

Fig. 11. Non-dimensional pressure drop $\Delta p^c/\Delta p^0$ as function of non-dimensional averaged velocity in constriction V^* for integral MGI model, differential approximation, and Carreau–Yasuda model.

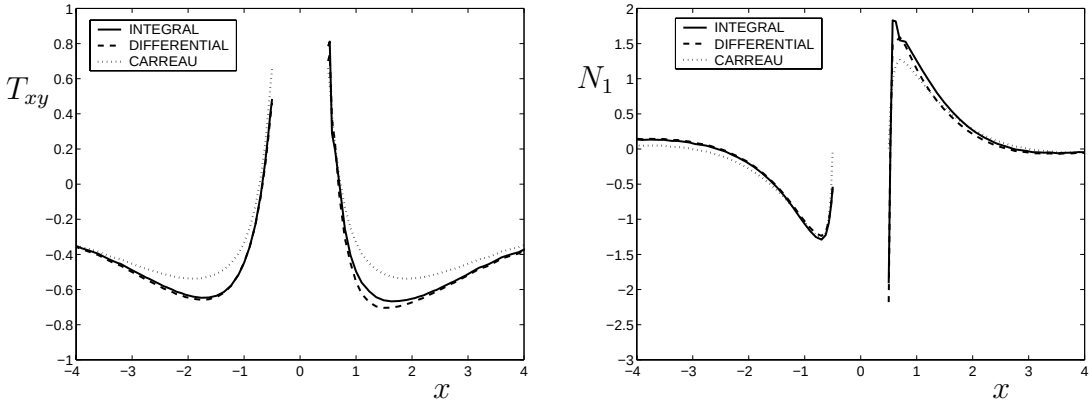

Fig. 12. Shear stress T_{xy} and normal stress N_1 along line $y = 3H/2$ at $We = 3$ for integral model, differential approximation, and Carreau–Yasuda model.

perfectly symmetric and antisymmetric, while for the viscoelastic models the stresses built up in the contraction part have not fully relaxed, so that a steeper stress boundary layer arises at the downstream side. This explains the closer resemblance upstream for the Carreau–Yasuda model. The differential approximation, however, captures the large stress gradients of the stresses in the boundary layer on the downstream side almost perfectly.

To examine the steady-state streamline patterns, we define the vortex intensity I_ψ, denoting the ratio of the amount of fluid flowing in the vortex and in the main flow. Setting the stream function value at the separating streamline equal

to zero, we have

$$I_\psi = -\frac{\psi_{cen}}{\psi_{ax}} \tag{17}$$

where ψ_{cen} and ψ_{ax} denote the values of the stream function at the centre of the vortex and the axis of symmetry, respectively. In Fig. 13 the streamlines and vortex intensities in steady state are displayed for the integral model, the differential approximation and the Carreau–Yasuda fit. For the lower Weissenberg number, both the streamlines in the vortex and the core flow are nearly symmetric in $x = 0$ as anticipated. The streamline patterns for the Newtonian limit $V^* \to 0$ are practically identical to the $V^* = 1$ Carreau–Yasuda case, with a slightly higher vortex intensity of $I_\psi = 7.4 \cdot 10^{-4}$. For the viscoelastic models, the symmetry no longer holds for the higher Weissenberg numbers. Then the streamlines in the expansion region of the core flow are shifted towards the downstream wall of the constriction. The vortices upstream and downstream of the constriction, however, mainly decrease in size and remain practically symmetric. Again, the differential equation for $\boldsymbol{T}^2$ well mimics the results of the integral model, except maybe for the vortex regions of $We = 10$ for which the differences in size and intensity are somewhat larger. Comparing with the streamlines of the Carreau–Yasuda model, however, shows similar streamline patterns as well, demonstrating the dominance of deformation thinning over the normal stresses and relaxation, absent in the Carreau–Yasuda model. The main difference is the absence of the shift of the streamlines towards the downstream constriction wall. The size of the vortices, however, remains remarkably similar, and only for the highest Weissenberg number when the vortex intensities are very small, the value of I_ψ for the Carreau–Yasuda model is considerably lower. Of course the transient leading towards the steady-state streamlines do differ from the Carreau–Yasuda model, which reaches steady state instantaneously.

5 Concluding remarks

By extending the numerical framework of Lagrangian particle methods with the deformation field method, we were able to accurately compute transient flow in a complex geometry using the integral MGI model. Without adding any solvent viscosity, high Weissenberg numbers could be reached in a 4:1:4 constriction flow. To achieve this, first a deficiency in the modeling of the convective constraint release had to be corrected, in order to avoid the unphysical situation of negative relaxation times. This situation arises for flows at higher Weissenberg numbers when the velocity gradient changes sign, while the stress does not due to its finite relaxation time. In the constriction geometry, this occurs in the expansion region, where we observed that the negative stress work

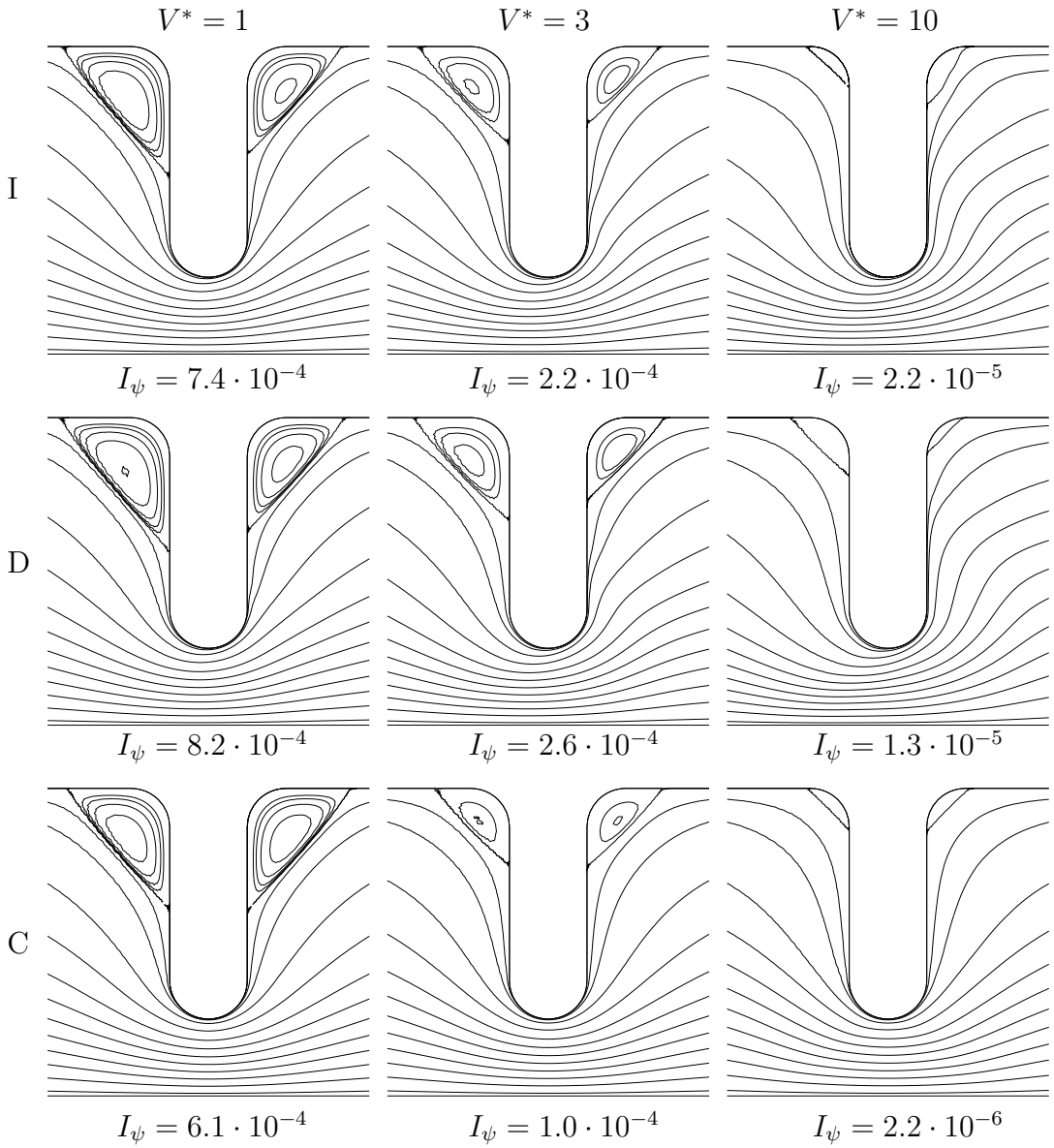

Fig. 13. Steady state streamlines and vortex intensities at various non-dimensional average velocities V^* for integral MGI model (I), differential approximation (D) and Carreau–Yasuda fit (C).

caused negative overall relaxation times, and consequently a negative memory function with increasing magnitude. Particularly for the integral model, negative relaxation times easily cause blow-up of the numerical scheme. To avoid this unphysical behaviour, we considered an ad hoc alternative for the CCR contribution to the relaxation time which is strictly positive.

In the constriction flow, for both low and high Weissenberg numbers, the approximate differential equation for the square of the polymer stress mimics the results of the integral MGI model very well. The close resemblance is not only

apparent for the steady state responses of streamlines and pressure drop but also for the stress transients. Especially in the contraction the results agree very well, while in the expansion some small differences arise. To investigate the influence of viscoelasticity in this flow, steady-state results have been compared with the Carreau–Yasuda model which only includes the shear-thinning behaviour. Unfortunately, the global kinematics like the streamlines and particularly the pressure drop are almost evenly well predicted by this much simpler inelastic model. And even the stress in the boundary layer is in good qualitative agreement.

Whether the present numerical results in complex flow represent real fluid flow behaviour or whether the model does not describe a linear polymer melt accurately enough, of course remains to be established. In case the model does not predict the correct behaviour, a natural choice seems to better model the extensional behaviour, which is dominated by a strong thinning for the MGI model. One possibility to do this, is to include tube stretch, similarly as for the Mead–Larson–Doi model [13]. If, on the other hand, the model does represent real polymer behaviour, our results raise the question whether such advanced rheological models are necessary to predict the behaviour of linear polymer melts in complex geometries.

Acknowledgements

This work is supported by the EC TMR contract FMRX-CT98-0210 and the ARC 97/02-210 project, Communauté Française de Belgique. We wish to thank Antony Beris, Giovanni Ianniruberto, Vincent Legat, and Pino Marrucci for discussions and helpful suggestions, and Xavier Gallez for providing the meshes. We also thank Martien Hulsen for sending us a preprint of [7]

References

[1] G. Marrucci, F. Greco, and G. Ianniruberto. Integral and differential constitutive equations for entangled polymers with simple versions of CCR and force balance on entanglements. *Rheol. Acta*, 2000. Submitted.

[2] M. Doi and S.F. Edwards. *The theory of polymer dynamics*. Clarendon Press, Oxford, 1986.

[3] G. Marrucci and N. Grizzuti. Fast flows of concentrated polymers: predictions of the tube model on chain stretching. *Gazz. Chim. Ital.*, 118:179–185, 1988.

[4] G. Ianniruberto and G. Marrucci. On compatibility of the Cox–Merz rule with the model of Doi and Edwards. *J. Non-Newtonian Fluid Mech.*, 65:241–246, 1996.

[5] T.C.B. McLeish and R.G. Larson. Molecular constitutive equations for a class of branched polymers: The pom-pom polymer. *J. Rheology*, 42:81–110, 1998.

[6] E.A.J.F. Peters, M.A. Hulsen, and B.H.A.A. van den Brule. Instationary Eulerian viscoelastic flow simulations using time separable Rivlin–Sawyers constitutive equations. *J. Non-Newtonian Fluid Mech.*, 89:209–228, 2000.

[7] E.A.J.F. Peters, A.P.G. van Heel, M.A. Hulsen, and B.H.A.A. van den Brule. Generalisation of the deformation field method to simulate advanced reptation models in complex flows. *J. Rheology*, 44:811–829, 2000.

[8] P. Wapperom, R. Keunings, and V. Legat. The backward-tracking Lagrangian particle method (BLPM) for transient viscoelastic flows. *J. Non-Newtonian Fluid Mech.*, 91:273–295, 2000.

[9] G. Marrucci. Private communication.

[10] R. Guénette and M. Fortin. A new mixed finite element method for computing viscoelastic flows. *J. Non-Newtonian Fluid Mech.*, 60:27–52, 1995.

[11] P. Halin, G. Lielens, R. Keunings, and V. Legat. The Lagrangian particle method for macroscopic and micro-macro viscoelastic flow computations. *J. Non-Newtonian Fluid Mech.*, 79:387–403, 1998.

[12] R.B. Bird, R.C. Armstrong, and O. Hassager. *Dynamics of polymeric liquids*, volume 1. John Wiley, New York, 2nd edition, 1987.

[13] D.W. Mead, R. Larson, and M. Doi. A molecular theory for fast flows of entangled polymers. *Macromolecules*, 31:7895–7914, 1998.